

See discussions, stats, and author profiles for this publication at: <https://www.researchgate.net/publication/279729928>

Infrared Spectroscopy of $\text{OH}\cdots\text{CH}_3\text{OH}$: Hydrogen-Bonded Intermediate Along the Hydrogen Abstraction Reaction Path

ARTICLE in THE JOURNAL OF PHYSICAL CHEMISTRY A · JULY 2015

Impact Factor: 2.69 · DOI: 10.1021/acs.jpca.5b04875 · Source: PubMed

CITATION

1

READS

43

5 AUTHORS, INCLUDING:



Federico Hernández

National University of Cordoba, Argentina

4 PUBLICATIONS 3 CITATIONS

SEE PROFILE



Gustavo A Pino

Universidad Nacional de Córdoba and CONICET

35 PUBLICATIONS 328 CITATIONS

SEE PROFILE

Infrared Spectroscopy of OH·CH₃OH: Hydrogen-Bonded Intermediate Along the Hydrogen Abstraction Reaction Path

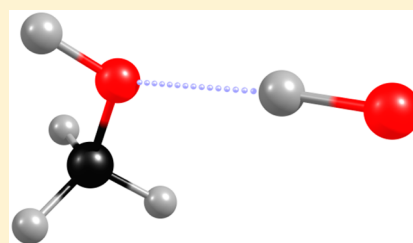
Federico J. Hernandez,^{†,‡} Joseph T. Brice,[†] Christopher M. Leavitt,[†] Gustavo A. Pino,[‡] and Gary E. Douberly^{*,†}

[†]Department of Chemistry, University of Georgia, Athens, Georgia 30602, United States

[‡]INFIQC, Dpto. de Fisicoquímica, Facultad de Ciencias Químicas, Centro Láser de Ciencias Moleculares, Universidad Nacional de Córdoba, Ciudad Universitaria, Pabellón. X5000HUA Córdoba, Argentina

S Supporting Information

ABSTRACT: Substantial non-Arrhenius behavior has been previously observed in the low temperature reaction between the hydroxyl radical and methanol. This behavior can be rationalized assuming the stabilization of an association adduct in the entrance channel of the reaction, from which barrier penetration via quantum mechanical tunneling produces the CH₃O radical and H₂O. Helium nanodroplet isolation and a serial pick-up technique are used to stabilize the hydrogen bonded prereactive OH·CH₃OH complex. Mass spectrometry and infrared spectroscopy are used to confirm its production and probe the OH stretch vibrations. Stark spectroscopy reveals the magnitude of the permanent electric dipole moment, which is compared to *ab initio* calculations that account for wide-amplitude motion in the complex. The vibrationally averaged structure has C_s symmetry with the OH moiety hydrogen bonded to the hydroxyl group of methanol. Nevertheless, the zero-point level of the complex exhibits a wave function significantly delocalized over a bending coordinate leading to the transition state of the CH₃O producing reaction.

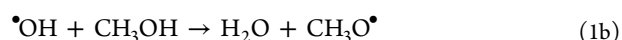
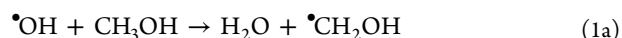


I. INTRODUCTION

The elimination of volatile organic compounds (VOCs) from the atmosphere is initiated by reactions with OH, NO₃, and O₃.^{1,2} For oxygenated VOCs, such as alcohols, ketones, ethers, etc., reaction occurs nearly exclusively with the hydroxyl radical.² Furthermore, the potential energy surface for the reaction between OH and an oxygenated VOC generally features a prereactive complex, stabilized by hydrogen bonding, which leads to a reaction rate that *increases* as the temperature is lowered.³ This was exquisitely demonstrated for the reaction between OH and methanol (MeOH), where the rate constant increased by nearly 2 orders of magnitude when the temperature decreased from ~200 K to below 70 K.^{4,5} In this study, we trap the prereactive complex formed between OH and MeOH using He nanodroplet isolation (HENDI) techniques,^{6–8} and probe this species using a combination of mass spectrometry and infrared (IR) laser Stark spectroscopy.

Over the past decade, airborne measurements of atmospheric composition have revealed high concentrations of VOCs in the free and upper troposphere, where they exert a significant impact on photochemistry.^{9–11} One of the most abundant oxygenated VOCs in the upper troposphere is MeOH,^{12,13} which is an important precursor to CO, formaldehyde, and ozone.¹¹ Its main sources are believed to be biogenic emissions, with smaller contributions from methane oxidation, biomass burning and damage/decay of flora.¹⁴ Hydroxyl radical initiated oxidation is accepted to be the major loss mechanism for atmospheric MeOH.² Several experimental^{4,5,15–17} and theoretical^{18,19} studies of the reaction between OH and MeOH

have probed its kinetics over a broad temperature range. The reaction can proceed via two competing pathways, corresponding to either a methyl-hydrogen (1a) or hydroxyl-hydrogen (1b) abstraction:



Reaction 1a is the dominant pathway at room temperature, which is expected on the basis of thermochemical data that show the methyl group to have the lower C–H bond dissociation energy.^{15–17} Many investigations have focused on accurately determining the product branching ratios for these two reactions at temperatures greater than 200 K.^{15–17} This was also the focus of a detailed theoretical study, where rate constants for 1a and 1b, as well as branching ratios, were calculated on the basis of an *ab initio* potential energy surface computed at the CCSD(T)/6-311+G(3df,2p)//MP2/6-311+G(3df,2p) level of theory.¹⁹ The potential energy surface for this reaction features a prereactive complex with a computed binding energy equal to 4.9 kcal·mol^{–1}. This rather large binding energy is derived from strong hydrogen bonding between the OH moiety and the hydroxyl group in MeOH. The reaction barriers on this potential surface are 1.0 and 3.6 kcal·mol^{–1} for pathways 1a and 1b, respectively, and channel 1a

Received: May 21, 2015

Revised: July 1, 2015

Published: July 2, 2015



at room temperature is predicted to account for $\approx 95\%$ of products.

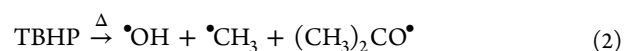
More recently, the kinetics of this system were studied at temperatures between 56 and 202 K, and substantial non-Arrhenius behavior was observed. At 56 K, an increase of nearly 2 orders of magnitude was observed in the overall reaction rate, in comparison to that measured at room temperature.^{4,5} Additionally, the higher energy pathway reaction 1b was *avored* at these lower temperatures, and this was rationalized as being due to the stabilization of the prereactive complex and subsequent quantum mechanical tunneling (QMT) through the reaction barrier. Despite the hydroxyl-hydrogen abstraction (1b) barrier being higher by ≈ 2.6 kcal·mol⁻¹, the barrier *width* is predicted¹⁹ to be significantly smaller than for abstraction of the methyl hydrogen atom (1a). At temperatures below 200 K, chemical master equation calculations incorporating QMT predict branching ratios favoring the CH₃O product, and this was rationalized as being due to the larger probability for H atom tunneling through the narrower barrier associated with pathway 1b.⁴ This dramatic change in the rate constant due to QMT at low temperatures implies the important role of prereactive complexes in the chemistry of the interstellar medium (ISM).⁴

The direct detection of the prereactive complex, formed between MeOH and OH, has proven elusive owing to the fleeting nature of this species. Helium droplets provide a means to trap reactive species, such as the OH·MeOH complex, where the energy released upon complex formation is rapidly dissipated by He atom evaporation. The resulting complex then equilibrates at the temperature of the droplet (i.e., 0.4 K), allowing for its spectroscopic study. Here we report the synthesis of the OH·MeOH complex within a He nanodroplet. We have probed the free and hydrogen bonded OH stretch modes of the complex with laser spectroscopy. The hydrogen bonded OH stretch is sufficiently resolved to allow for an analysis of its dipole moment via Stark spectroscopy. The experimental data is analyzed in the context of electronic structure calculations. Stark spectroscopy reveals a wide-amplitude bending motion of the OH radical within the complex and a rather significant complexation-induced dipole moment, both of which are relevant for a detailed understanding of the QMT at play in this prototypical system.

II. EXPERIMENTAL METHODS

Helium nanodroplet isolation (HENDI) is a well-established technique for studying the spectroscopy of molecules.^{6–8} A custom apparatus at the University of Georgia, consisting of three differentially pumped chambers, was used to record IR spectra of the hydroxyl-methanol (OH·MeOH) complex. Helium droplets were generated by continuously expanding high pressure He (~ 30 bar) into vacuum through a 5 ± 1 μ m aperture cooled to 16 K. The resulting droplets were cooled to ~ 0.4 K, via He atom evaporation,²⁰ and skimmed into a beam. Using known scaling laws,²¹ He droplets formed within this source consist of approximately 5000 atoms; droplets of this size can dissipate nearly 72 kcal·mol⁻¹.

The OH·MeOH complex was formed within a He droplet using a serial pick-up process. First, the He droplet beam passed in front of an effusive pyrolysis source comprised of a quartz tube, the tip of which (~ 0.5 mm in length) was wrapped with a resistively heated tantalum wire. Hydroxyl radicals were generated from the pyrolysis of *tert*-butyl hydrogen peroxide (TBHP):²²



Fragmentation of the precursor is nearly complete above 800 °C, and the droplets have an equal probability of picking up a hydroxyl, methyl, or acetone molecule. Next, the droplets passed through a 2 cm long, differentially pumped pick-up cell (PUC) filled with MeOH vapor. Unless otherwise stated, the pressure of MeOH was maintained at $\sim 2.5 \times 10^{-6}$ Torr, which optimized the pick-up of a single MeOH molecule, a value that was empirically determined from PUC pressure dependence curves (*vide infra*). The droplet beam then traversed a Stark/multipass cell,^{23,24} where the embedded chromophores were subjected to IR radiation supplied by a continuous wave, optical parametric oscillator (B-module, Aculight). The tuning and calibration of this laser system is described elsewhere.²⁵ The Stark cell consists of two parallel gold-coated mirrors situated orthogonal to two stainless steel electrodes to which a static electric field can be applied for Stark spectroscopy. The doped droplet beam was then analyzed with an off-axis electron impact quadrupole mass spectrometer. Upon vibrational excitation, the energy deposited into the embedded cluster is quenched by statistical evaporation of He atoms (~ 5 cm⁻¹ per atom) from the droplet. This leads to a reduction in the geometrical and ionization cross-section of the doped He droplet, which is ultimately observed as a decrease in the ion-signal in the mass spectrum.

III. THEORETICAL METHODS

All electronic structure calculations were performed at the uMP2/aug-cc-pVTZ level of theory using the Gaussian09 package.²⁶ The geometries and harmonic frequencies were computed for OH, MeOH, and the OH·MeOH complex. The optimized geometry of the complex is in agreement with that predicted by Lin and co-workers at the CCSD(T)/6-311+G-(3df,2p)//MP2/6-311+G(3df,2p) level of theory.¹⁹ Anharmonic frequencies were also calculated for the complex and MeOH using VPT2 (as implemented in Gaussian09) to determine the cubic and quartic force constants at the same level. The results from frequency calculations are summarized in Table 1.

Table 1. Vibrational Band Origins in the OH Stretching Region (cm⁻¹)

	OH·MeOH		MeOH	OH
	H-bonded OH	free OH		
harmonic	3619	3860	3859	3794
anharmonic	3487	3699	3686	3642 ^a
expt	3445.0	3684	3685	3568

^aScaled harmonic frequency; scale factor 0.9598.

IV. RESULTS AND DISCUSSION

Iva. Mass Spectrometry. Figure 1 presents a series of mass spectra illustrating the sequential steps leading to the formation of the OH·MeOH complex in He droplets. The mass spectrum of the neat He droplet beam is found in Figure 1a. A series of mass peaks separated by 4 u are assigned to (He)_n⁺ clusters that are generated via the ionization and fragmentation of pure He droplets. A peak at 18 u is also observed, and this signal is derived from background water molecules that are picked up by the droplet beam. Figure 1b presents the mass spectrum when

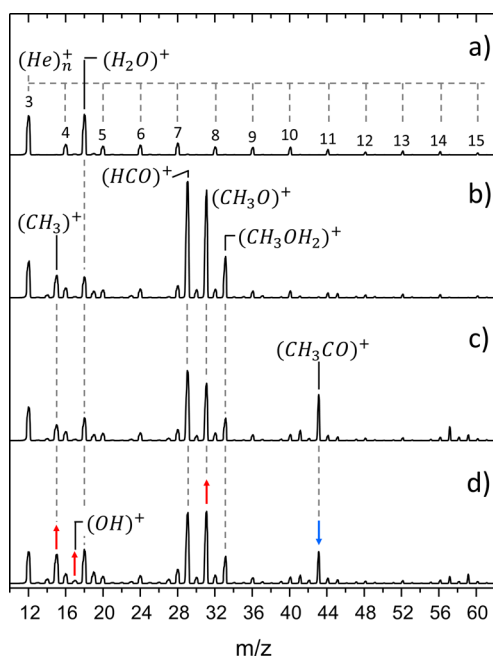


Figure 1. Mass spectra of the droplet beam: (a) neat droplet beam; (b) MeOH-doped droplet beam; (c) MeOH-doped droplet beam with TBHP flowing through the room temperature pyrolysis source; (d) MeOH-doped droplet beam with TBHP flowing through the ~ 1000 $^{\circ}\text{C}$ pyrolysis source. The red and blue arrows indicate mass peaks that qualitatively change upon heating the pyrolysis source.

the PUC is filled with MeOH vapor to 2.5×10^{-6} Torr. A series of MeOH fragment ions are present in this mass spectrum. This type of fragmentation is quite typical for He-solvated molecules,^{6,7} where ionization of the droplet gives rise to He^+ , which can charge-transfer ionize the dopant.²⁷ Because of the approximately 14 eV difference between the He ionization potential and that of the dopant, the molecular ion generated via this mechanism undergoes fragmentation similar to that observed in gas-phase electron impact ionization mass spectrometry. Figure 1, parts c and d, are mass spectra recorded following the serial pick-up of TBHP and MeOH when the pyrolysis source was operated at room temperature and ~ 1000 $^{\circ}\text{C}$, respectively. The primary mass peak indicative of TBHP pick-up is $m/z = 43$ u. As the temperature of the pyrolysis source increases, the ion signal on this mass channel decreases (indicated by the blue arrow in Figure 1d), with a concomitant increase of ion signal in channels $m/z = 15$ (CH_3^+), 17 (OH^+), and 31 u (CH_3O^+). The former two channels have been shown to carry ion signal depletion in the spectroscopy of the methyl radical²⁸ and the hydroxyl radical,²² both of which are pyrolysis products of TBHP. Although we did not observe a unique mass channel arising from the formation and subsequent ionization of the $\text{OH}\cdots\text{MeOH}$ complex, the small increase in 31 u under high temperature pyrolysis conditions motivated the acquisition of survey IR spectra as ion current depletion in this mass channel.

IVb. Vibrational Spectroscopy of $\text{OH}\cdots\text{MeOH}$. A survey vibrational spectrum through the OH stretch region was recorded under conditions in which droplets sequentially picked-up room temperature TBHP and MeOH (Figure 2a), whereas the spectrum in Figure 2b was obtained with the pyrolysis source operated near ~ 1000 $^{\circ}\text{C}$. Both spectra were collected by monitoring the laser-induced depletion of $m/z = 31$ u, and the raw signal is presented (not normalized to laser

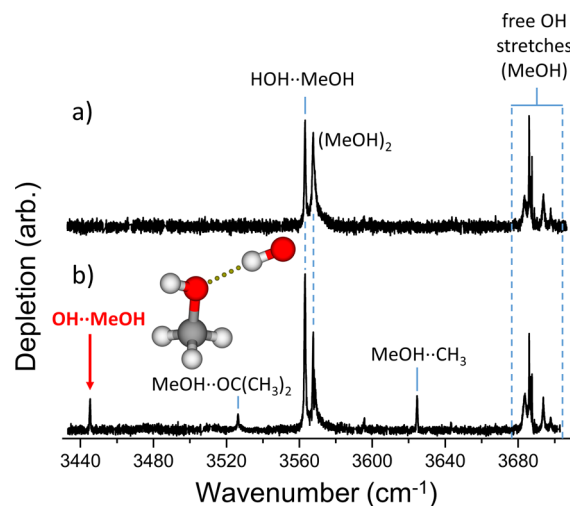


Figure 2. Survey spectra of the (a) MeOH doped droplet beam recorded with the TBHP precursor flowing through the room temperature pyrolysis source. The $\text{HOH}\cdots\text{MeOH}$ complex is present due to the pick-up of water molecules that originate from the TBHP sample. (b) Spectra recorded under identical conditions but with the pyrolysis source heated to ~ 1000 $^{\circ}\text{C}$. The three new bands in the hydrogen bonded OH stretch region are assigned to $\text{MeOH}\cdots\text{CH}_3$, $\text{MeOH}\cdots\text{O}=\text{C}(\text{CH}_3)_2$, and $\text{OH}\cdots\text{MeOH}$ complexes (high to low frequency), all of which have an equal probability of being synthesized within the He droplets. The minimum energy geometry at the uMP2/aug-cc-pVTZ level of theory is shown as the inset.

power) in both cases. Because a substantial fraction of droplets are doped with only a single MeOH molecule, we expect to observe the rovibrational ν_1 band (OH stretch) of MeOH, the spectrum of which was recently reported in He droplets.²⁹ Indeed the transitions associated with the ν_1 band of MeOH are located near 3690 cm^{-1} in both spectra. Moreover, intense bands at 3563 and 3567 cm^{-1} are present in both spectra. Two likely candidates for the latter two vibrational bands are the hydrogen bonded MeOH dimer and the water-MeOH complex, where the water originates from the incompletely dried TBHP sample. Gas-phase, jet-cooled FT-IR spectra of pure and mixed complexes of MeOH and H_2O have previously been reported,³⁰ and the gas-phase vibrational bands assigned to the hydrogen bonded OH stretches of $\text{HOH}\cdots\text{MeOH}$ and $(\text{MeOH})_2$ are within 4 and 8 cm^{-1} of the bands at 3563 and 3567 cm^{-1} in the droplet spectrum, respectively. We therefore make similar assignments, as indicated in Figure 2.

Three prominent features at 3445 , 3526 , and 3624 cm^{-1} are clearly dependent upon the temperature of the pyrolysis source (Figure 2b). At this stage of the analysis, these features are tentatively assigned to complexes containing MeOH and the pyrolysis products of TBHP. The three pyrolysis products of TBHP, presented in eq 2, give rise to the $\text{MeOH}\cdots\text{CH}_3$, $\text{MeOH}\cdots\text{O}=\text{C}(\text{CH}_3)_2$, and $\text{OH}\cdots\text{MeOH}$ complexes, all of which have an equal probability of being synthesized within He droplets. To identify the transitions associated with the methyl and acetone containing complexes, we performed the same experiment, but instead, we used di-*tert*-butyl peroxide (DTBP) as the pyrolysis precursor. DTBP thermally decomposes into two methyl radicals and two acetone molecules, whereas it does not produce the hydroxyl radical. The two bands centered at 3526 and 3624 cm^{-1} are also present in the spectrum recorded using the DTBP precursor (Figure S1), and these bands are assigned to the hydrogen

bonded OH stretches of $\text{MeOH}\cdots\text{O}=\text{C}(\text{CH}_3)_2$ and $\text{MeOH}\cdots\text{CH}_3$, respectively. However, this spectrum does not contain the lowest frequency band at 3445 cm^{-1} , and we therefore assign this band to the hydrogen bonded OH stretch of the $\text{OH}\cdots\text{MeOH}$ complex.

The computed minimum energy geometry of the $\text{OH}\cdots\text{MeOH}$ complex is presented in the inset of Figure 2b. At this geometry, the hydroxyl radical is the H-bond donor, with the oxygen atom of MeOH acting as the acceptor. We therefore expect hydrogen bonded and free OH stretching modes localized on the hydroxyl radical and MeOH fragments, respectively. The corresponding harmonic and anharmonic frequencies of these vibrations are collected in Table 1. The H-bonded OH stretch is predicted to be within 42 cm^{-1} of the experimental 3445 cm^{-1} band when anharmonic corrections are computed with vibrational perturbation theory (VPT2). Although not definitive, this anharmonic frequency calculation, which apparently under-predicts the complexation induced red shift, is at least consistent with our assignment of this band to the H-bonded OH stretch of the $\text{OH}\cdots\text{MeOH}$ complex.

Upon formation of the hydrogen bonded complex, harmonic and anharmonic calculations also predict, respectively, blue shifts of 1 and 13 cm^{-1} for the free OH stretch on the MeOH moiety. This makes it particularly challenging to experimentally identify the free OH stretch of the complex, as the ν_1 band of He-solvated MeOH contains 10 transitions spanning $3684\text{--}3698\text{ cm}^{-1}$.²⁹ Furthermore, it was determined that the broad transition centered at 3683.5 cm^{-1} was due to the free OH stretch of larger $(\text{MeOH})_n$ clusters.²⁹ Considering the free OH stretch bands, it is reasonable to expect comparable complexation induced frequency shifts for $(\text{MeOH})_2$ and $\text{OH}\cdots\text{MeOH}$, which have similar hydrogen bonded geometries. The free OH stretch of the latter complex could contribute to the broad transition at 3683.5 cm^{-1} , as there is no other band in this vicinity that can be assigned to $\text{OH}\cdots\text{MeOH}$. To test this hypothesis, we collected PUC curves, with the results presented in the inset of Figure 3. Pressure dependence curves for the optimal pick-up of one and two MeOH molecules were generated by monitoring the bands at 3693.79 and 3567.71

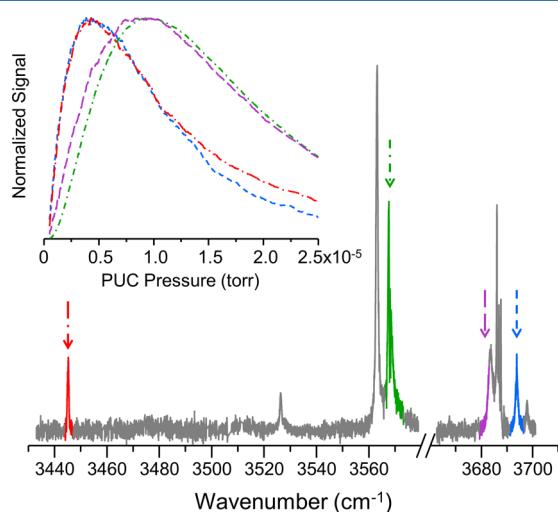


Figure 3. Pick-up cell pressure dependence curves; color indicates the fixed laser frequency. The MeOH monomer (blue) curve and the $\text{OH}\cdots\text{MeOH}$ curve (red) almost exactly overlap. Signal intensity on the 3683.5 cm^{-1} band has a pressure dependence intermediate between that of the methanol monomer (blue) and dimer (green).

cm^{-1} , respectively (highlighted in blue and green in Figure 3). The depletion signals at these frequencies are optimized at PUC pressures equal to 4.2×10^{-6} and 9.5×10^{-6} Torr, respectively. As expected, the signal due to the MeOH dimer peaks at approximately twice the optimal pressure for the monomer. For the band assigned to the H-bonded OH stretch of $\text{OH}\cdots\text{MeOH}$ (red trace in Figure 3), the PUC curve follows almost exactly the curve generated for the MeOH monomer, consistent with the aforementioned assignment. Interestingly, the PUC curve generated with the laser tuned to 3682.72 cm^{-1} (highlighted in violet in Figure 3) peaks at a slightly lower pressure than the optimal pressure determined for the pick-up of two MeOH molecules. Moreover, the leading edge of this curve lies between those for MeOH and $(\text{MeOH})_2$, perhaps indicating the contribution of a complex containing a single MeOH molecule to the broad feature at 3683.5 cm^{-1} .

Figure 4 presents a series of IR spectra over the free OH stretching region. The pressure of the PUC was maintained at

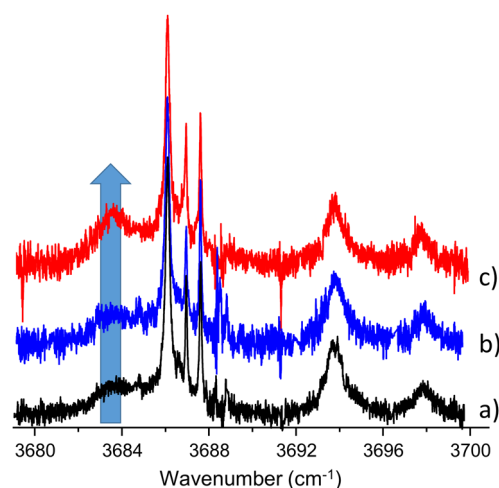


Figure 4. Free OH stretch region of the methanol monomer. All features above 3685 cm^{-1} are due exclusively to the monomer. The broad feature centered near 3683.5 cm^{-1} is attributed to the methanol dimer. The intensity of the broad feature is similar in spectra a and b, which were recorded under identical conditions. In spectrum a, only MeOH is present in the pick-up chamber, whereas in part b the TBHP precursor is flowing through the room temperature pyrolysis source (see Figure 2a). In spectrum c, the pyrolysis source is heated to $\sim 1000^\circ\text{C}$. The intensity of the 3683.5 cm^{-1} feature grows in intensity upon heating the pyrolysis source, thus upon producing the hydroxyl radical and the $\text{OH}\cdots\text{MeOH}$ complex.

$\sim 5 \times 10^{-7}$ Torr, which substantially reduces the probability for forming $(\text{MeOH})_2$ clusters via the sequential pick-up of two MeOH molecules. The spectrum obtained with only MeOH present in the PUC is shown in Figure 4a, which provides a baseline spectrum of the MeOH monomer at these experimental conditions. While the broad feature centered at 3683.5 cm^{-1} is present, the relative intensity with respect to the free OH stretch transitions of isolated MeOH has decreased compared to the spectrum in Figure 2a. A nearly identical spectrum (Figure 4b) is obtained when TBHP is introduced into the pick-up chamber with the pyrolysis source operated near room temperature. Figure 4c presents the spectrum recorded with the pyrolysis source temperature at $\sim 1000^\circ\text{C}$. The transitions derived from the ν_1 band of MeOH are relatively insensitive to the temperature of the pyrolysis source, as expected. However, the intensity of the broad transition at

3683.5 cm^{-1} increases, as indicated by the arrow in Figure 4. The pyrolysis source temperature dependence and the PUC curves suggest an assignment of the 3683.5 cm^{-1} band to the free OH stretch of OH·MeOH, although, in addition to (MeOH)₂, the free OH stretch of HOH·MeOH is also likely contributing to the signal at this frequency.

IVc. Stark Spectroscopy of OH·MeOH. The PUC pressure dependence curves clearly show that the carrier of the 3445 cm^{-1} band contains a single MeOH molecule. Moreover, its frequency shift and dependence on pyrolysis source conditions support the assignment of this band to the hydrogen bonded OH stretch within the OH·MeOH complex. A slower scan over this vibrational band reveals partially resolved rotational structure that can be further analyzed, as shown at the bottom of Figure 5. A rigid, asymmetric rotor

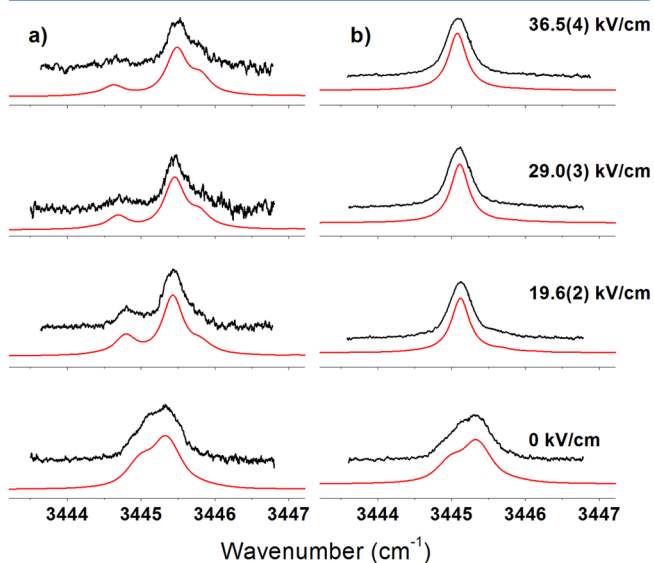


Figure 5. Zero-field and Stark spectra of the hydrogen bonded OH stretch band of the OH·MeOH complex. The zero-field spectra along the bottom exhibit a rotational contour that can be simulated with an asymmetric top model parametrized by the constants given in Table 2. The Stark simulations are produced using the zero-field rotational constants and the computed expectation values of the inertial dipole components for the OH·MeOH complex (see text). The Stark simulations are in excellent agreement with the experiment for all field strengths and both laser polarization configurations (perpendicular, a; parallel, b), providing convincing evidence for the assignment of the 3445 cm^{-1} band.

analysis via a contour fitting procedure in PGOPHER³¹ gives the associated rotational constants, $A = 0.67$ and $(B+C)/2 = 0.04$ cm^{-1} . When compared to *ab initio* values for the C_s symmetry OH·MeOH geometry (Table 2), the experimental A and $(B+C)/2$ constants are 1.8 and 3.3 times smaller, respectively. Rotational constants of He-solvated molecular systems are typically reduced by a factor of 2 to 3 from gas-phase values, when comparisons are available.^{6,7} The helium solvent contributes to the effective moment of inertia of the molecular rotor, hence the rotational constant renormalization.

The above rotational contour analysis assumes that the electronic orbital angular momentum of the OH radical is fully quenched as a result of the strong hydrogen bonding interaction present in the complex.^{32–34} This assumption is validated by calculations at the CIS(D)/aug-cc-pVTZ//uMP2/aug-cc-pVTZ level, which predict an ~ 1100 cm^{-1} energy

Table 2. Rotational Constants (cm^{-1}) and Dipole Moment Components (Debye) Used in Rovibrational Zero-Field and Stark Simulations^a

OH·MeOH	simulation	constrained potential	relaxed potential ^b	C_1 (Minimum)	C_s (TS)
A	0.67 ^c			1.165	1.207
B	0.04 ^c			0.138	0.136
C	0.04 ^c			0.126	0.125
$\langle \mu_a \rangle$	3.9	3.95	3.92	4.02 ^d	4.08 ^d
$\langle \mu_b \rangle$	0.8	0.80	0.78	0.801 ^d	0.886 ^d
$\langle \mu_c \rangle$	0	0	0	0.489 ^d	0.0 ^d

^aThe hydrogen bonded OH stretch band in the OH·MeOH complex is an a -/ b -hybrid band. The ratio of transition dipole moment projections onto the inertial a - and b -axes is $(\mu_a/\mu_b) = 4.8$. This value is equivalent to that computed for the hydrogen bonded OH stretch band at the minimum energy geometry. The band origin in the simulations is 3445.13 cm^{-1} , and the rovibrational transitions are convoluted with a 0.3 cm^{-1} Lorentzian line width. ^bWe note that similar dipole moment calculations employing a relaxed potential energy scan (relaxed bond lengths and angles of the OH and MeOH fragments) give results that are essentially the same as those from the constrained potential surface. ^cRotational constants are reduced from computed values on account of the helium's contribution to the rotor's effective moment of inertia. Here, $(B+C)/2 = 0.04$ cm^{-1} . ^dEquilibrium components of the dipole moment at the C_1 minimum energy ($\phi \approx 15^\circ$) and C_s transition state ($\phi = 0^\circ$) geometries.

difference between the spin–orbit coupled $^2A'$ and $^2A''$ states. These lowest lying electronic states differ in the orientation of the singly occupied $p\pi$ orbital relative to the symmetry plane of the C_s symmetry OH·MeOH complex. Each rovibrational transition is convoluted with a Lorentzian line shape function having a full-width at half-maximum equal to 0.3 cm^{-1} . The laser bandwidth is substantially less than this line width, and the broadening observed for the 3445 cm^{-1} band is likely due to a homogeneous vibrational deactivation mechanism related to the relatively strong hydrogen bonding present in this system. In large part due to this broadening, simulations employing the angular momentum quenching model in refs 32–34 are not sensitive to the $A' - A''$ energetic separation once it is larger than about 500 cm^{-1} . Therefore, the assumption that the hydroxyl radical orbital angular momentum is quenched upon complexation with MeOH should be acceptable for the analysis of the partially resolved rotational contour observed here.

Although consistent with our assignment, the analysis of the zero-field rotational contours is not definitive. We also measured several Stark spectra of the 3445 cm^{-1} band, which are shown in Figure 5, parts a and b, for perpendicular and parallel laser polarization configurations, respectively. Unlike rotational constants, it has been shown that the dipole moments of He-solvated molecules are nearly identical to those in the gas-phase,²³ and we can much more confidently compare the dipole moments extracted from He droplet spectra to those computed with *ab initio* theory.²⁴ The Stark spectrum at each electric field strength was simulated using the rotational constants determined from the zero-field spectrum (Table 2). At all field strengths, and for both laser polarization configurations, the agreement between experiment and simulation is excellent when the magnitude of μ_a and μ_b are fixed to 3.9 and 0.8 D, respectively. The perpendicular polarization spectra (Figure 5a) are particularly sensitive to the a - component of the dipole moment. This strongly supports the assignment of this band to the hydrogen bonded

OH stretch within the OH·MeOH complex, which has computed equilibrium dipole components $\mu_a = 4.02$ D and $\mu_b = 0.80$ D.

The experimental Stark spectra necessarily probe the expectation values of the inertial dipole components. To explore the effect of wide-amplitude motion on the OH·MeOH dipole moment, a one-dimensional potential energy surface was constructed by varying the O(1)–O(2)–C–H(3) dihedral angle, ϕ (Figure 6). The OH bond axis was

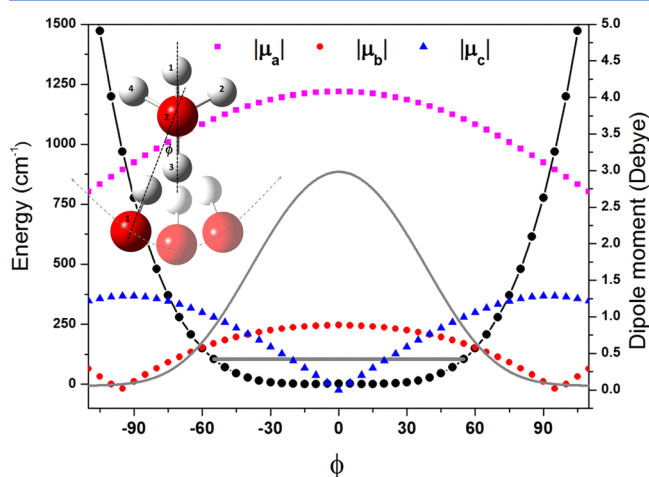


Figure 6. One-dimensional potential energy surface (black) constructed by varying the O(1)–O(2)–C–H(3) dihedral angle, ϕ , while keeping all other degrees of freedom fixed. The OH bond axis was constrained to point along the line connecting the two O atoms. The structure is presented as a top-down view, with the O–C bond pointing into the page. With $\phi = 0$, the complex has C_s symmetry. The mirror plane contains the OH moiety and the O(2), H(1), C and H(3) atoms on MeOH. The electronic structure calculation predicts the C_s structure to be a transition state, although the barrier between the two equivalent C_1 minima is only 15 cm^{-1} . The zero-point energy is 104.3 cm^{-1} . The absolute values of the inertial dipole components (pink, red, and blue) were averaged using the square of the ground-state wave function (gray) obtained from a Cooley–Numerov calculation. By symmetry, the expectation value of μ_c is zero because its sign changes in going from positive to negative values of ϕ .

constrained to point along the line connecting the two O atoms, and all other degrees of freedom were kept fixed. This coordinate was chosen because it captures the large-amplitude bending motion of the OH moiety with respect to the H(3)CO(2)H(1) plane. Indeed, the lowest frequency vibration computed for the C_1 symmetry equilibrium structure is almost entirely projected onto this distinguished reaction coordinate. The grid points in the potential were calculated every 5 degrees from $\phi = 0^\circ$ to $\phi = 120^\circ$. The final potential was completed by taking advantage of symmetry, $V(\phi) = V(-\phi)$. The minimum energy geometry has C_1 symmetry with $\phi \approx \pm 15^\circ$. The geometry at $\phi = 0^\circ$ corresponds to a transition state with C_s symmetry, where the normal coordinate associated with the imaginary frequency is also approximately coincident with the distinguished reaction coordinate chosen here. The potential barrier is 15 cm^{-1} above the two equivalent C_1 minima, as determined from fully relaxed geometry optimizations of the C_1 and C_s configurations. The potential was interpolated using an eighth order polynomial fit to generate a finer grid for use in a Cooley–Numerov algorithm adapted from Levine.³⁵ The reduced mass used for the Numerov program was taken from

the single imaginary frequency associated with the C_s structure. It is evident from the solution of the 1D Schrödinger equation that the vibrationally averaged structure is effectively C_s , with the zero-point level located 89 cm^{-1} above the barrier. Nevertheless, the wave function is significantly delocalized over ϕ . Interestingly, this wide-amplitude bending motion is in the direction of the transition state to reaction 1b, and zero-point motion along this coordinate is expected to impact the analysis of QMT in this system.

At each point in the potential, the dipole moment components were obtained from the MP2 density matrix in the inertial frame. The square of the computed ground state wave function was used to calculate the expectation value of the magnitude of each inertial dipole moment component (Table 2). For free MeOH, the a -axis is approximately along the C–O bond, and the b -axis lies perpendicular to the C–O bond and in the COH plane. Upon complex formation with OH, the a - and b -axes remain in the mirror plane of the complex (assuming C_s symmetry), and the c -axis is perpendicular to this plane. By symmetry, the expectation value of μ_c is zero, because its sign changes in going from positive to negative values of ϕ . The expectation values of μ_a and μ_b are 3.95 and 0.80 D, respectively, which are in excellent agreement with experiment. Despite the wide-amplitude motion present in the complex, vibrational averaging has only a minor effect on the a - and b -components of the dipole moment, as these are relatively insensitive to motion along ϕ in the vicinity of the C_s structure.

The dipole moment of OH is 1.67 D ,²² and the dipole moment of MeOH has components $\mu_a = 0.89$ and $\mu_b = 1.43\text{ D}$.³⁶ It is interesting to note that the magnitude of $\langle \mu \rangle$ in the complex (4.03 D) is significantly larger than the sum of the dipole moments of the monomers ($\mu_{\text{MeOH}} + \mu_{\text{OH}} = 3.30\text{ D}$), implying a complexation-induced dipole moment of $\sim 0.73\text{ D}$. From the Stark spectroscopy and theoretical analysis presented here, we can conclude that the 3445 cm^{-1} band derives from a carrier having a vibrationally averaged C_s structure and a permanent dipole moment equal to $\sim 4.0\text{ D}$. This C_s symmetry structure had not been previously considered in theoretical studies of this prototypical system.

V. CONCLUSIONS

A hydrogen-bonded complex between the hydroxyl radical and methanol was formed in He droplets via the sequential pick-up of the monomers. IR spectroscopy in the OH stretch region reveals bands at 3445.1 and 3683.5 cm^{-1} that can be assigned, respectively, to the H-bonded and free OH stretches localized on the OH and MeOH moieties within the complex. The red-shifted H-bonded stretch exhibits partially resolved rotational structure, which has been probed with Stark spectroscopy. The experimental rotational contours measured at several electric field strengths are in excellent agreement with predictions from *ab initio* theory that take into account a wide-amplitude bending motion in the complex. The vibrationally averaged geometry of the OH·MeOH complex is C_s symmetry, with the OH radical hydrogen bonded to the hydroxyl group of MeOH (Figure 6). Nevertheless, the potential energy surface for OH bending relative to the COH plane in MeOH is rather flat, with only a 15 cm^{-1} barrier between equivalent C_1 minima. For this reason, the calculated ground-state wave function in this potential is significantly delocalized. Future high-level computations of reaction rates and their temperature dependence, which take into account QMT, will necessarily have to consider the zero-point energy associated with the wide-amplitude

motion discussed here. Indeed, this degree of freedom corresponds approximately to the minimum energy pathway between the hydrogen bonded complex and the transition state for hydroxyl-hydrogen abstraction, which leads to the production of $\text{CH}_3\text{O} + \text{H}_2\text{O}$.

■ ASSOCIATED CONTENT

■ Supporting Information

Figure S1, survey spectrum of MeOH plus the pyrolysis products of DTBP. The Supporting Information is available free of charge on the ACS Publications website at DOI: 10.1021/acs.jpca.5b04875.

■ AUTHOR INFORMATION

Corresponding Author

*(G.E.D.) E-mail: douberty@uga.edu. Telephone: 01-706-542-3857.

Notes

The authors declare no competing financial interest.

■ ACKNOWLEDGMENTS

G.E.D. acknowledges support from the National Science Foundation (CHE-1054742). G.A.P acknowledges CONICET, FONCYT and SeCyT-UNC for financial support.

■ REFERENCES

- (1) Atkinson, R.; Arey, J. Atmospheric Degradation of Volatile Organic Compounds. *Chem. Rev.* **2003**, *103*, 4605–4638.
- (2) Mellouki, A.; Le Bras, G.; Sidebottom, H. Kinetics and Mechanisms of the Oxidation of Oxygenated Organic Compounds in the Gas Phase. *Chem. Rev.* **2003**, *103*, 5077–5096.
- (3) Smith, I. W. M.; Ravishankara, A. R. Role of Hydrogen-Bonded Intermediates in the Bimolecular Reactions of the Hydroxyl Radical. *J. Phys. Chem. A* **2002**, *106*, 4798–4807.
- (4) Shannon, R. J.; Blitz, M. A.; Goddard, A.; Heard, D. E. Accelerated Chemistry in the Reaction between the Hydroxyl Radical and Methanol at Interstellar Temperatures Facilitated by Tunnelling. *Nat. Chem.* **2013**, *5*, 745–749.
- (5) Martin, J. C. G.; Caravan, R. L.; Blitz, M. A.; Heard, D. E.; Plane, J. M. C. Low Temperature Kinetics of the $\text{CH}_3\text{OH} + \text{OH}$ Reaction. *J. Phys. Chem. A* **2014**, *118*, 2693–2701.
- (6) Toennies, J. P.; Vilesov, A. F. Superfluid Helium Droplets: A Uniquely Cold Nanomatrix for Molecules and Molecular Complexes. *Angew. Chem., Int. Ed.* **2004**, *43*, 2622–2648.
- (7) Choi, M. Y.; Douberty, G. E.; Falconer, T. M.; Lewis, W. K.; Lindsay, C. M.; Merritt, J. M.; Stiles, P. L.; Miller, R. E. Infrared Spectroscopy of Helium Nanodroplets: Novel Methods for Physics and Chemistry. *Int. Rev. Phys. Chem.* **2006**, *25*, 15–75.
- (8) Stienkemeier, F.; Lehmann, K. K. Spectroscopy and Dynamics in Helium Nanodroplets. *J. Phys. B: At., Mol. Opt. Phys.* **2006**, *39*, R127–R166.
- (9) Singh, H. B.; Kanakidou, M.; Crutzen, P. J.; Jacob, D. J. High-Concentrations and Photochemical Fate of Oxygenated Hydrocarbons in the Global Troposphere. *Nature* **1995**, *378*, 50–54.
- (10) Singh, H.; Chen, Y.; Staudt, A.; Jacob, D.; Blake, D.; Heikes, B.; Snow, J. Evidence from the Pacific Troposphere for Large Global Sources of Oxygenated Organic Compounds. *Nature* **2001**, *410*, 1078–1081.
- (11) Singh, H. B.; Salas, L. J.; Chatfield, R. B.; Czech, E.; Fried, A.; Walega, J.; Evans, M. J.; Field, B. D.; Jacob, D. J.; Blake, D.; et al. Analysis of the Atmospheric Distribution, Sources, and Sinks of Oxygenated Volatile Organic Chemicals Based on Measurements over the Pacific During Trace-P. *J. Geophys. Res.* **2004**, *109*, D15S07.
- (12) Cady-Pereira, K. E.; Shephard, M. W.; Millet, D. B.; Luo, M.; Wells, K. C.; Xiao, Y.; Payne, V. H.; Worden, J. Methanol from Tes Global Observations: Retrieval Algorithm and Seasonal and Spatial Variability. *Atmos. Chem. Phys.* **2012**, *12*, 8189–8203.
- (13) Wells, K. C.; Millet, D. B.; Hu, L.; Cady-Pereira, K. E.; Xiao, Y.; Shephard, M. W.; Clerbaux, C. L.; Clarisse, L.; Coheur, P. F.; Apel, E. C.; et al. Tropospheric Methanol Observations from Space: Retrieval Evaluation and Constraints on the Seasonality of Biogenic Emissions. *Atmos. Chem. Phys.* **2012**, *12*, 5897–5912.
- (14) Harley, P.; Greenberg, J.; Niinemets, U.; Guenther, A. Environmental Controls over Methanol Emission from Leaves. *Biogeosciences* **2007**, *4*, 1083–1099.
- (15) Dillon, T. J.; Hölscher, D.; Sivakumaran, V.; Horowitz, A.; Crowley, J. N. Kinetics of the Reactions of HO with Methanol (210–351 K) and with Ethanol (216–368 K). *Phys. Chem. Chem. Phys.* **2005**, *7*, 349–355.
- (16) Hägele, J.; Lorenz, K.; Rhäsa, D.; Zellner, R. Rate Constants and CH_3O Product Yield of the Reaction $\text{OH} + \text{CH}_3\text{OH} \rightarrow \text{Products}$. *Ber. Bunsen Phys. Chem.* **1983**, *87*, 1023–1026.
- (17) Meier, U.; Grotheer, H. H.; Just, T. Temperature-Dependence and Branching Ratio of the $\text{CH}_3\text{OH} + \text{OH}$ Reaction. *Chem. Phys. Lett.* **1984**, *106*, 97–101.
- (18) Galano, A.; Alvarez-Idaboy, J. R.; Bravo-Perez, G.; Ruiz-Santoyo, M. E. Gas Phase Reactions of $\text{C}_1\text{--C}_4$ Alcohols with the OH Radical: A Quantum Mechanical Approach. *Phys. Chem. Chem. Phys.* **2002**, *4*, 4648–4662.
- (19) Xu, S.; Lin, M. C. Theoretical Study on the Kinetics for OH Reactions with CH_3OH and $\text{C}_2\text{H}_5\text{OH}$. *Proc. Combust. Inst.* **2007**, *31*, 159–166.
- (20) Hartmann, M.; Miller, R. E.; Toennies, J. P.; Vilesov, A. Rotationally Resolved Spectroscopy of SF_6 in Liquid-Helium Clusters: A Molecular Probe of Cluster Temperature. *Phys. Rev. Lett.* **1995**, *75*, 1566–1569.
- (21) Knuth, E.; Schilling, B.; Toennies, J. P. *Proceedings of the 19th International Symposium on Rarefied Gas Dynamics*; Oxford University Press: London, 1995.
- (22) Raston, P. L.; Liang, T.; Douberty, G. E. Anomalous Lambda-Doubling in the Infrared Spectrum of the Hydroxyl Radical in Helium Nanodroplets. *J. Phys. Chem. A* **2013**, *117*, 8103–8110.
- (23) Stiles, P. L.; Nauta, K.; Miller, R. E. Dipole Moments of Molecules Solvated in Helium Nanodroplets. *Phys. Rev. Lett.* **2003**, *90*, 135301.
- (24) Liang, T.; Magers, D. B.; Raston, P. L.; Allen, W. D.; Douberty, G. E. Dipole Moment of the HOOO Radical: Resolution of a Structural Enigma. *J. Phys. Chem. Lett.* **2013**, *4*, 3584–3589.
- (25) Morrison, A. M.; Liang, T.; Douberty, G. E. Automation of an "Aculight" Continuous-Wave Optical Parametric Oscillator. *Rev. Sci. Instrum.* **2013**, *84*, 013102.
- (26) Frisch, M. J.; Trucks, G. W.; Schlegel, H. B.; Scuseria, G. E.; Robb, M. A.; Cheeseman, J. R.; Scalmani, G.; Barone, V.; Mennucci, B.; Petersson, G. A.; et al. *Gaussian 09*, Revision D.01; Gaussian Inc.: Wallingford, CT, 2009.
- (27) Scheidemann, A.; Schilling, B.; Toennies, J. P. Anomalies in the Reactions of He^+ with SF_6 Embedded in Large ^4He Clusters. *J. Phys. Chem.* **1993**, *97*, 2128–2138.
- (28) Morrison, A. M.; Raston, P. L.; Douberty, G. E. Rotational Dynamics of the Methyl Radical in Superfluid ^4He Nanodroplets. *J. Phys. Chem. A* **2013**, *117*, 11640–11647.
- (29) Raston, P. L.; Douberty, G. E.; Jäger, W. Single and Double Resonance Spectroscopy of Methanol Embedded in Superfluid Helium Nanodroplets. *J. Chem. Phys.* **2014**, *141*, 044301.
- (30) Nedić, M.; Wassermann, T. N.; Larsen, R. W.; Suhm, M. A. A Combined Raman- and Infrared Jet Study of Mixed Methanol-Water and Ethanol-Water Clusters. *Phys. Chem. Chem. Phys.* **2011**, *13*, 14050–14063.
- (31) Western, C. M. *PGOPHER, a Program for Simulating Rotational Structure*, 8.0; University of Bristol Research Data Repository: Bristol, U.K., 2014.
- (32) Marshall, M. D.; Lester, M. I. Spectroscopic Implications of the Coupling of Unquenched Angular Momentum to Rotation in OH-Containing Complexes. *J. Chem. Phys.* **2004**, *121*, 3019–3029.

(33) Marshall, M. D.; Lester, M. I. Spectroscopic Implications of Partially Quenched Orbital Angular Momentum in the OH-Water Complex. *J. Phys. Chem. B* **2005**, *109*, 8400–8406.

(34) Douberly, G. E.; Raston, P. L.; Liang, T.; Marshall, M. D. Infrared Rovibrational Spectroscopy of OH-C₂H₂ in ⁴He Nanodroplets: Parity Splitting Due to Partially Quenched Electronic Angular Momentum. *J. Chem. Phys.* **2015**, *142*, 134306.

(35) Levine, I. N. *Quantum Chemistry*, 6th ed.; Pearson Prentice-Hall: Upper Saddle River, NJ, 2009.

(36) Sastry, K. V. L. N.; Vanderlinde, J.; Donovan, D.; Mukhopadhyay, I.; Gupta, P. K. Determination of the Dipole-Moment of C-13 Methanol by Microwave Stark Spectroscopy. *J. Mol. Spectrosc.* **1994**, *168*, 374–383.